Numerical Simulation of Shock Interactions

Numerical Simulation of Shock Interactions

DOMENIC D'AMBROSIO and MAURIZIO PANDOLFI
Politecnico di Torino - Dipartimento di Ingegneria Aerospaziale
Corso Duca degli Abruzzi, 24 - 10129 Torino - ITALY
E-Mail: domenic@athena.polito.it - pandolfi@polito.it
Fax: +39 011 5646899

Summary

In this paper we present the results of numerical simulations on shock/boundary layer and on shock/shock interactions. The shock/boundary layer interaction is investigated on a hollow-cylinder-flare configuration, while the shock/shock interaction is obtained from the interference of the shock generated by a ramp with the bow shock about a cylinder. We will underline the most delicate points that one must consider in carrying out such computations and we will compare our numerical results with experimental data for purposes of validation.

1 Introduction

The enormous progress in computer sciences and the parallel development and improvement of computational methods has made of our days CFD a very powerful tool. In principle, linking sufficient computer power with the most efficient numerical methods available, it is possible to simulate the flowfield about very complex configurations obtaining, in many cases, solutions which are sufficiently accurate to give useful information to designers.

Actually, a number of points remains open: turbulence, for instance, is still far to be adequately simulated in practical applications, and so is transition. This lack is not only due to the CFD numerical methods themselves, but also to the missing of adequate models (DNS is still too far from practical applications). Analogous issues are present in combustion problems and in the simulation of thermochemical effects in high speed flows.

Today, we may say that CFD is like a young adult, with a lot still to learn, but with good potential capabilities. A very important point to notice is that CFD is also trying to become *mature*. We envisage this search for maturity in the fact that the CFD community is concentrating an important part of its time to check, in apparently simple test cases, its own capabilities and limits. This is true for the whole community, and is

especially important in the high speed regime, where the validation process mutually involves the experimental side also.

In the present contribution, we would like to show some examples which are related to the numerical simulation of shock/boundary layer and shock/shock interactions in high speed laminar flows and their comparison with experiments. They are part of the activities carried out in a sequel of high speed flow-field databases [1][2] and they are also studied in the NATO/RTO Working Group 10, Subgroup 3, whose subject is "CFD Validation". Our aim is to show that despite the simple geometrical configurations and the fact that the flow is cold and in the laminar regime (so that no model is required in addition to the Navier-Stokes equations), these configurations still hide difficult points that make it not trivial to obtain solutions that fit with other numerical results and with experimental data.

2 Numerical method

The results that we will present have been obtained using a well established numerical technique, whose details, which we will not describe here, can be found, for instance, in references [3][4][5]. In synthesis, we solve the Navier-Stokes equations for two-dimensional axisymmetric flows. The numerical method adopts a finite volume discretisation of the physical domain, an explicit integration scheme, a flux difference splitting technique for the evaluation of the convective fluxes and a standard cell centered method for diffusive fluxes. For some computations, a multi-block domain decomposition method was used. Finally, we reach a nominal second order accuracy in space and time using and Essentially Non Oscillating scheme.

3 Shock wave/boundary layer interactions.

The first configuration that we wish to consider is the so called *Hollow Cylinder Flare*. Such a configuration is used to validate axisymmetric strong shock/boundary layer interactions in the laminar regime at very low density and at high speed. Experiments on an identical Hollow Cylinder Flare geometry and in similar flow conditions have been carried out in France by ONERA (R5Ch tunnel)[1] and very recently in the USA, at CALSPAN (Veridian 48" tunnel)[6]. The geometrical setup is presented in figure 1.

We start with describing the results obtained for the ONERA test configuration, whose flow conditions are listed in the upper left table of figure 5. Computations have been performed using a grid composed of 99x299 points in the normal and tangential directions, respectively. Points are equally spaced in the x-direction, with a constant $\Delta(x/L) = 0.57471 \times 10^{-2}$. In the normal direction, the grid is stretched with many mesh points clustered close to the wall. In order to estimate the scale of the grid cells in relation with flow conditions, the dimensionless distance from the wall of the first cell center has been computed. Distance y^+ is defined as:

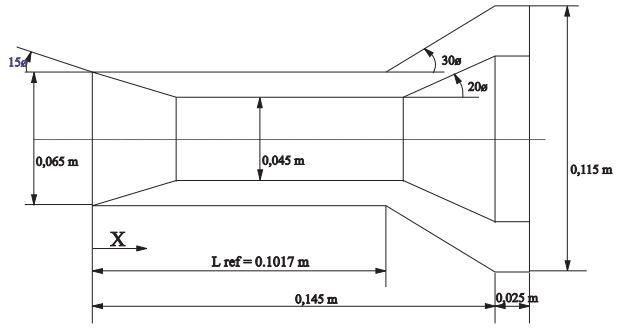

Figure 1 Geometrical setup for the Hollow Cylinder Flare configuration.

$$y^+ = \frac{y u_\tau}{\nu} = \frac{\hat{y}\hat{u}_\tau}{\hat{\nu}} \sqrt{\frac{Re_{L_\infty}}{\sqrt{\gamma} M_\infty}} \tag{3.1}$$

$$u_\tau = \sqrt{\frac{|\tau_w|}{\rho_w}} \quad \text{and} \quad \hat{u}_\tau = \sqrt{\frac{|\hat{\tau}_w|}{\hat{\rho}_w}} \tag{3.2}$$

The quantity $\hat{u}_\tau$ is the so called "friction velocity" [7]. We have computed values of $y^+(I,J=1)$ smaller than 0.24 along the entire wall and below 0.06 for most part of it, including the recirculation bubble region, and we are therefore confident that the grid that we use is sufficiently refined.

Due to the low Reynolds number and the high Mach number, a thick viscous layer develops on the cylinder wall and deviates the incoming particles upstream. As a consequence, a shock wave starts at the leading edge of the cylinder. Since the growth rate of the viscous layer decreases while proceeding downstream, also the shock intensity diminishes.

At the corner, the total pressure loss suffered through the leading edge shock and inside the viscous layer deprives slower particles flowing in the near-wall region of the momentum needed to climb the 30 degrees flare angle. A separation bubble provides to re-shape the cylinder/flare intersection with a smoother slope and also anticipates the influence of the corner to a region where the total pressure is higher. Of course, this causes a complete change in the flowfield. In normal conditions, a system of compression wavelets merging in a shock wave immediately outside the subsonic part of the viscous layer should exist at the corner. In the present case, instead, it is substituted by two less intense compression wavelets/shock systems. The first one starts in front of the separation point and is due to the presence of the bubble; the second one is created before the reattachment area, where the bubble upper boundary increases its slope with respect to the incoming flow to prepare to match with the flare slope. The three shock converge almost in the same point and since the strongest is the one generated near the reattachment area (the leading edge shock is very weak), it dictates the slope of the resulting shock. The latter will be subsequently weakened by the expansion fan generated at the corner between the flare and the second larger cylinder, in an area which is not of

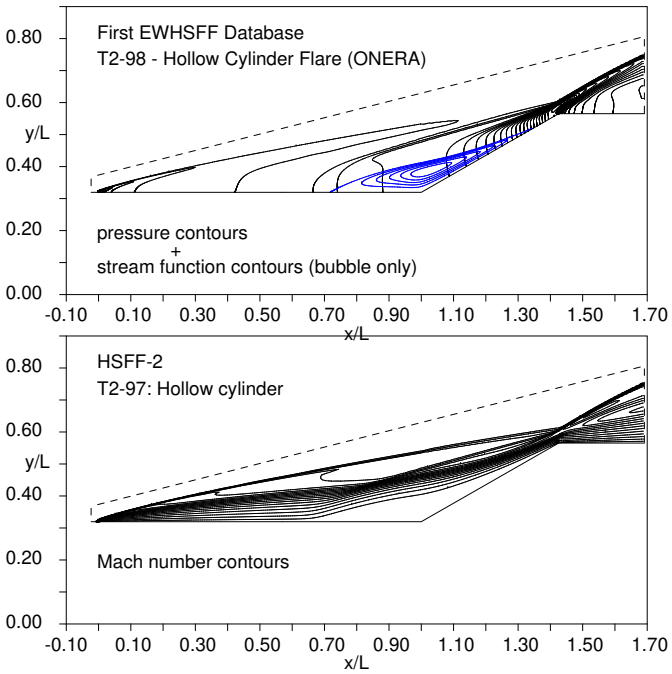

Figure 2 Top: pressure contours and streamlines (bubble only). Bottom: Mach number contours.

great interest for the present investigation.

The flow characteristics described above can be appreciated in figure 2(top), where pressure contours and stream function contours are overlaid (the latter are plotted for the separated region only). Mach number contours are shown in figure 2(bottom); though not very significative, they indicate that the separation bubble is a definitely low speed region.

Computed pressure coefficient and Stanton number are shown in figures 3a and 3b as a function of x/L. They are compared with experimental results obtained at ONERA. The agreement is satisfactory, except for the fact that the pressure levels are a little smaller in the experiment than in the computation.

The skin friction coefficient is presented in figure 3c. Separation and reattachment points lay where c_f has a null value. In the present study, the computed value is $x/L = 0.717$ for the separation point and $x/L = 1.348$ for the reattachment point. The presence of the separation bubble and its upstream influence are clearly evidenced in the c_p plot, also. The Stanton number curve is less easily interpretable, but the presence of the separation is recognizable in the change of slope at about $x/L \simeq 0.7$.

All the three coefficients peak at the end of the flare, where reattachment occurs, and than suddenly decrease due to the expansion starting at the leading edge of the second cylinder corner. The intensity of such peaks, especially the one of the Stanton number, is an important parameter to determine the reliability of a numerical simulation. The

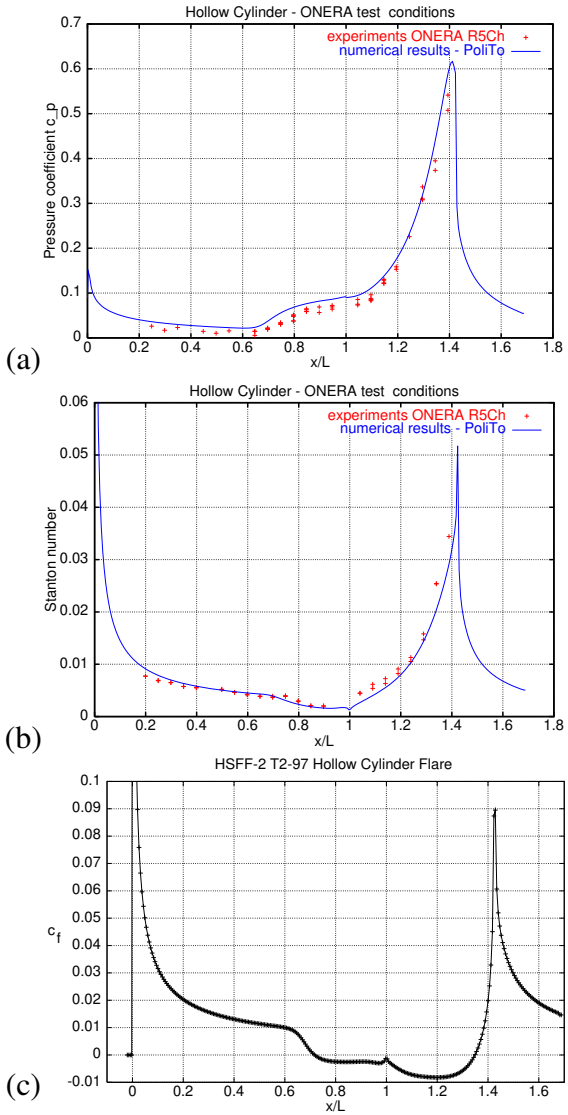

Figure 3 Hollow cylinder/flare, ONERA conditions: (a)pressure coefficient, (b)Stanton number and (c)skin friction coefficient.

fact that the reattachment point is so close to the end of the flare rises the suspicion that, in this case, the flare length might control the bubble dimension.

The principal problem in reproducing the flow around the hollow cylinder/flare configuration consists in the correct capturing of the recirculation region at the corner between the cylinder and the flare. Such an issue can be related, up to a certain extent, to the ability possessed by the investigating tool of predicting the effectiveness of maneu-

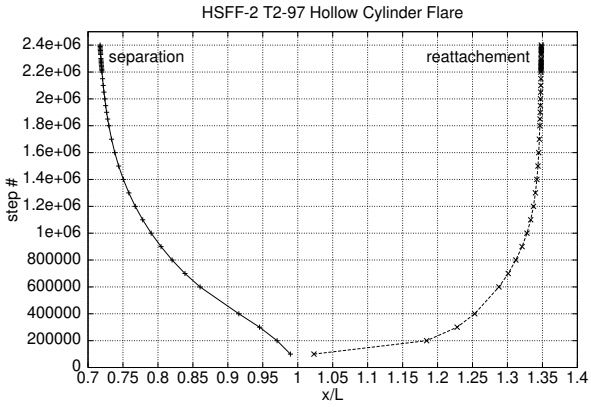

Figure 4 Separation bubble growth history.

verig surfaces in more realistic vehicle configurations.

From the numerical simulation point of view, two major elements characterize the investigation of the hollow cylinder/flare configuration. The first is the need for high accuracy in order to capture the steep gradients that occur in correspondence with the recirculation region. The second is the necessity of performing many time iterations before the recirculation region reaches a steady state regime, a problem which is related to the slow convection of vorticity inside the viscous layer and the separation bubble.

The correct numerical capture of the separation bubble represents a delicate problem, being grid-dependent and very time consuming. The grid used in the present computation appears to be sufficiently fine to assure a correct evaluation of the amplitude of the recirculation region, but such a strong refinement implies also rather long computing times. The size of the bubble is in fact dictated by the convection of vorticity along the boundary layer, which is the slowest part of the flowfield. The growth of the bubble amplitude versus the number of integration steps is shown in figure 4. The computation was performed in this case using a global time stepping approach, in order to evidence the very slow growing rate of the bubble.

We now proceed to presenting the results obtained in simulating the hollow cylinder/flare configuration in the CALSPAN flow conditions, which are listed in the table included in figure 5. The grid is identical to the one used for the ONERA test conditions; in this case, we have computed values of y^+ for the first cell centers which are smaller than 1.5 for the entire model wall and below 0.24 for most part of it. The dimensionless distance from the wall is larger in the CALSPAN test conditions because, in this case, the density at the wall is definitely smaller than in the ONERA test conditions. Here, we will not present any comparison with the experiments conducted at CALSPAN, because the latter are currently under way. Qualitatively, the flowfield features are the same of the ONERA test case, but the details, which are important in this kind of investigation, are very different. Indeed, the comparison between the numerical results obtained simulating the ONERA and the CALSPAN experiments is instructive, as it shows that very different results can be obtained for the same geometry and for

Hollow Cylinder Flare (ONERA)		
M_∞	=	9.91
Re_∞	=	1.86×10^5 m^{-1}
T^o_∞	=	1050 K
T_∞	=	50.87 K
T_{wall}	=	293 K
L	=	0.1017 m

Hollow Cylinder Flare (CALSPAN)		
M_∞	=	9.555
Re_∞	=	1.426×10^5 m^{-1}
T^o_∞	=	3217 K
T_∞	=	194.1 K
T_{wall}	=	297.8 K
L	=	0.1017 m

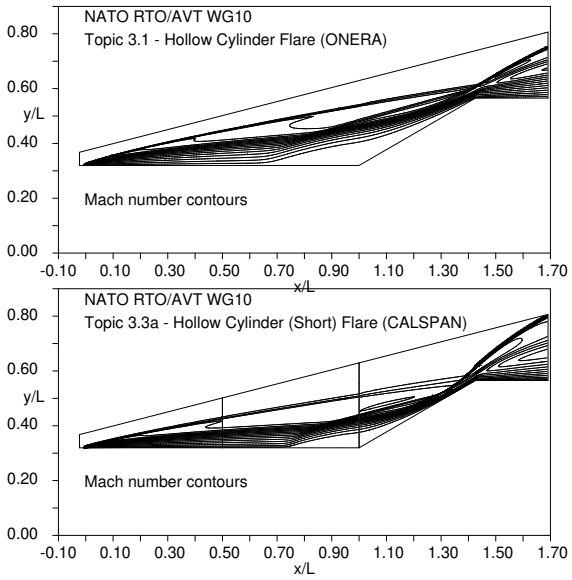

Figure 5 Hollow Cylinder: Mach number contours in the ONERA and CALSPAN test conditions.

experimental conditions that, at a first glance, look very similar. In the present case, for instance, two identical models are used, and the incoming flow conditions are very close in terms of Mach number and Reynolds number. The only difference regards the ratio T_w/T_∞, which differs by almost thrice in the two test-cases. From the results that we obtained, we learned that the parameter T_w/T_∞ is very important for this kind of flow. A larger T_∞ and the same Mach number mean a larger speed for the incoming flow, and therefore, being the Reynolds number the same, also a thinner boundary layer

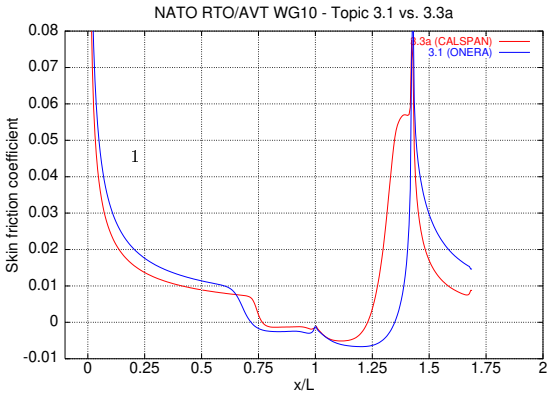

Figure 6 Skin friction coefficieht in the ONERA and CALSPAN conditions.

and thus a smaller recirculation region. Such features are evident in figures 5 and 6, where the Mach number contours and the skin friction coefficients are compared for the two configurations.

We mentioned previously that in the ONERA flow conditions the reattachment point of the recirculation region almost coincides with the end of the flare. Though this is not the case for the smaller bubble which appears in the CALSPAN conditions, a further

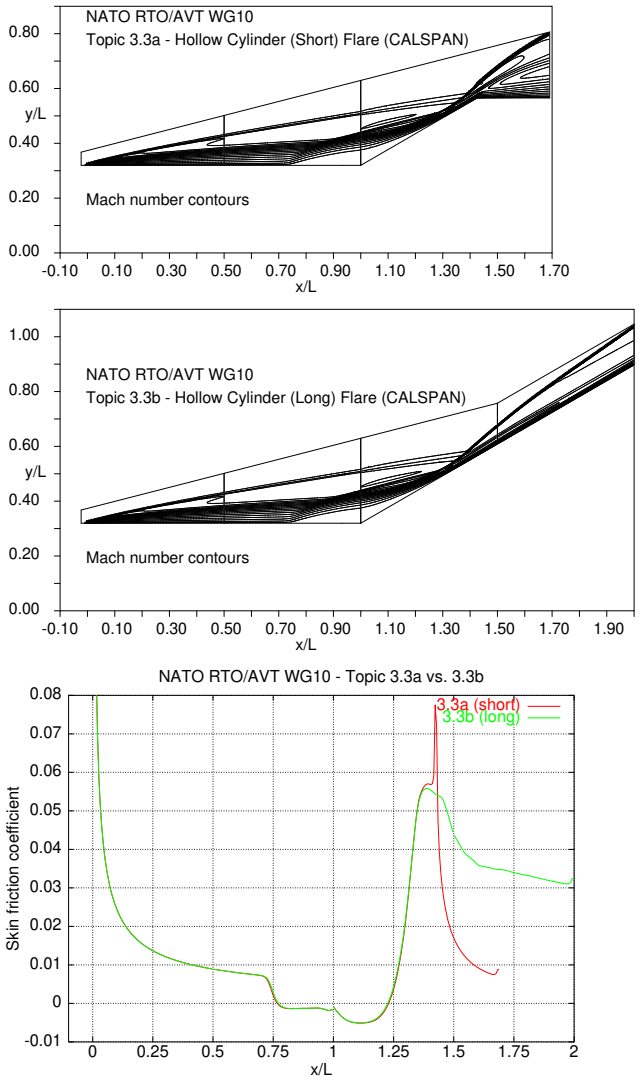

Figure 7 Top: Mach number contours for the ONERA configuration. Middle: Mach number contours for the CALSPAN configuration. Bottom: comparison between the skin friction coefficients.

experiment has been designed at CALSPAN to check the influence of the flare length on the bubble size. With this aim, the hollow-cylinder configuration has been tested in the CALSPAN conditions using a longer flare. The result of the experiment is that no influence at all is detected, as it can be evinced from the skin friction coefficient curves plotted in figure 7. Therefore we can conclude that the flare length is an effective control parameter only when the bubble extension would be larger then it, but it has no influence in the opposite case. We plan to compute in the future the "long flare" version of the Hollow Cylinder Flare configuration in the ONERA flow conditions, to check whether the flare length affects the size of the recirculation bubble in this case.

4 Shock/shock interactions.

The second shock interaction that we will consider is an *oblique-shock/bow-shock interaction* tested by ONERA in the R5Ch tunnel. Flow conditions and geometrical setup are shown in figure 8.

The interaction of an oblique shock wave with the bow shock about a circular cylinder is interesting, from an engineering point of view, because it simulates, in a simple way, the same kind of flowfield that might be present in the interaction between the external compression oblique shock and the cowl in a hypersonic intake, or between the fuselage shock and the fin shock.

From the physical point of view, the fluid dynamics structures that may arise from the interaction might be, depending on the strength of the two shocks, very complex and intriguing, and are still not completely described in detail.

In particular, the present test case deals with a so called *Edney-type IV interaction*, that results in a supersonic jet that impinges on the surface of the cylinder and produces an heat flux peak that exceeds by an order of magnitude the maximum heat flux that should be predicted in absence of the interaction. The correct prediction of such an heat flux is of course vital for design purposes.

Shock/shock interaction		
M_∞	=	9.95
Re_∞	=	167237 m^{-1}
T_∞	=	52.5 K
T_{wall}	=	300 K
R_{cyl}	=	0.008 m

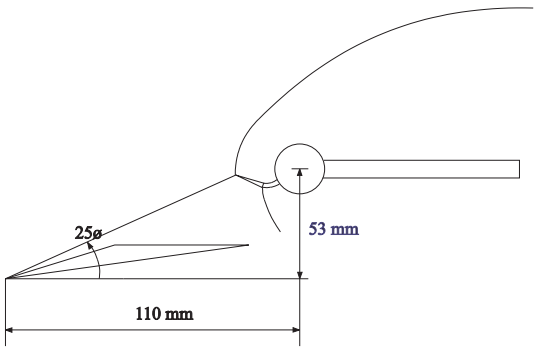

Figure 8 Flow conditions and geometrical setup for the shock/shock interaction.

From the numerical simulation point of view, the major difficulties are related to the different scales that characterize the flowfield structures. The supersonic jet and the wave interactions that occur inside it are small with respect to the cylinder radius, and the cylinder radius, at least in the sent case, is small with respect to the dimensions of the oblique shock generator. Thus, a highly accurate scheme and a good grid refinement strategy are required for a successful simulation.

We have learned from some preliminary computations that the determination of the exact position and inclination of the impinging shock is fundamental for a faithful reproduction of the experimental tests. In particular, due to the smallness of the cylinder radius with respect to the shock generator characteristic length, a slight difference in the inclination of the impinging shock may result in a non-negligible variation of the stagnation point position. The situation in sketched in figure 9. Moreover, due to the small Reynolds number, the flow in the high pressure side of the oblique shock, which will play an important role in the interaction, is not uniform. For these reasons, it has been deemed necessary to compute the entire flowfield generated by the wedge and to use it as boundary condition for the mesh surrounding the cylinder.

Computations have been performed using one grid for the upper part of the shock generator, one grid for the lower part, one grid for the stream past the shock generator and finally a grid composed of 300x351 points in the normal and tangential directions, respectively, for the cylinder. All the grids are stretched in the normal direction close to the solid walls. The mesh around the cylinder is refined with stretching also in the region of the supersonic jet. The external boundaries of the four grids used are visible in figure 9.

In order to estimate the scale of the grid cells in relation with flow conditions, the dimensionless distance from the wall y^+ of the first cell centers has been computed. The plot, not included here for lack of space, shows that first cells centers lay at distances

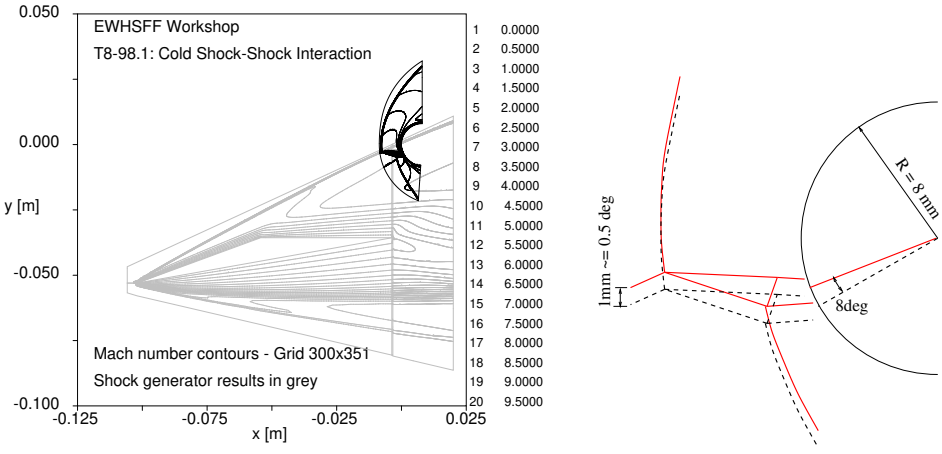

Figure 9 Shock/shock interaction: complete configuration (left); the effect of the incident shock position on the stagnation point sketch (right).

$y^+ \leq 0.2$ for most part of the cylinder walls, and reach the maximum value of 0.74 in correspondence with the stagnation point. Thanks to this analysis and to preliminary investigations with coarser grids, we are confident that the grid convergence has been reached.

In the present test case, the intersection between the incident oblique shock generated by the wedge and the detached shock which forms ahead of the cylinder takes place where the bow shock is strong (subsonic flow in the high pressure side). The interaction belongs to the Edney-type IV family [8] and is characterized by the presence of a supersonic jet surrounded by subsonic flow. In principle, a repeated pattern of expansions and compressions develops inside the jet channel, but in this case, due to the vicinity of the jet to the cylinder wall, we can distinguish only a few of them. In particular, from the analysis of our results, we interpret the flowfield inside the jet as sketched in figure 10b). The shock wave at the "entrance" the supersonic channel is irregularly reflected from the upper slip line and forms a λ-shock. In correspondence with the reflection point, an expansion fan forms to permit to part of the streamlines to flow slightly upwards. At the opposite side of the jet, the second leg of the $lambda$-shock interacts with

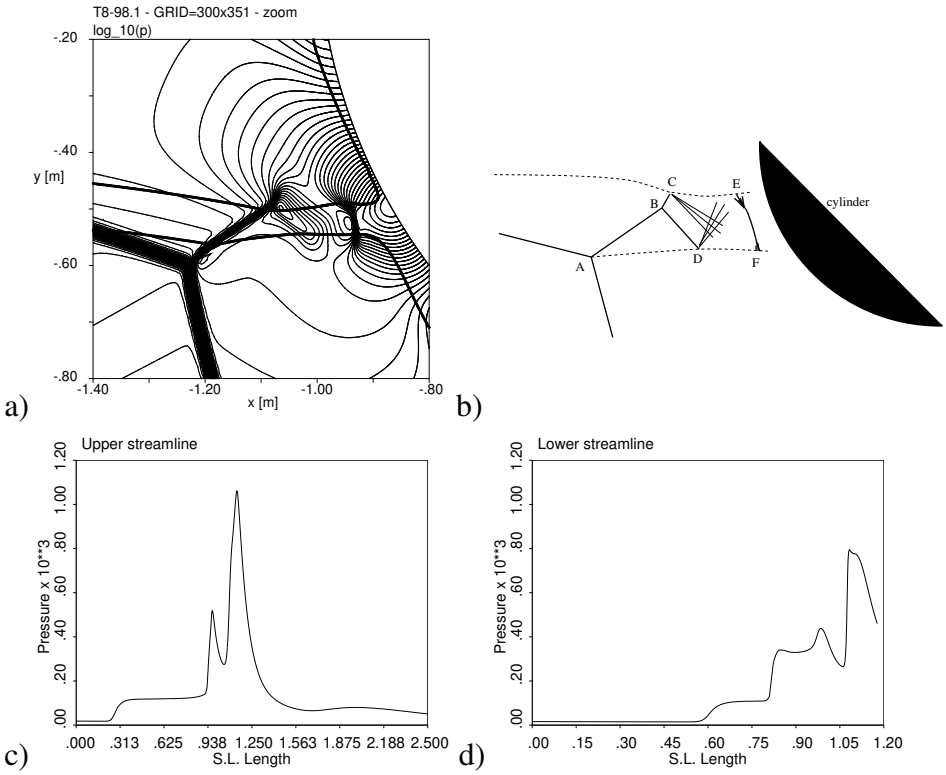

Figure 10 a)Log_{10} of pressure contours with streamlines, b)interpretation of the wave pattern inside the jet, c)pressure variations along the upper streamline, d) pressure variations along the lower streamline.

the lower slip line and is reflected as an expansion fan, which deviates part of the jet slightly downwards. Approaching the body, the supersonic stream which flows inside the jet is suddenly decelerated through a detached shock. The jet is finally divided in two streams which flow upward and downward the stagnation point. The previous interpretation arise from the study of figure 10, where log_{10} of pressure plots are shown in part a), with the paths of two streamlines superimposed. In figures 10c) and 10d), the pressure conditions along these streamlines are displayed. It can be noticed that, after the pressure rise due to the oblique Mach shock, a second increase in pressure, due to the shock at the "entrance" of the channel, is present. This second pressure rise is stronger and unique for the upper streamline, which crosses the λ-shock practically at the triple point, while it is less intense, and followed by a second compression for the lower streamline, which crosses the two legs of the λ-shock. Then, both streamlines experience a pressure drop due to the expansions fans and finally a strong compression

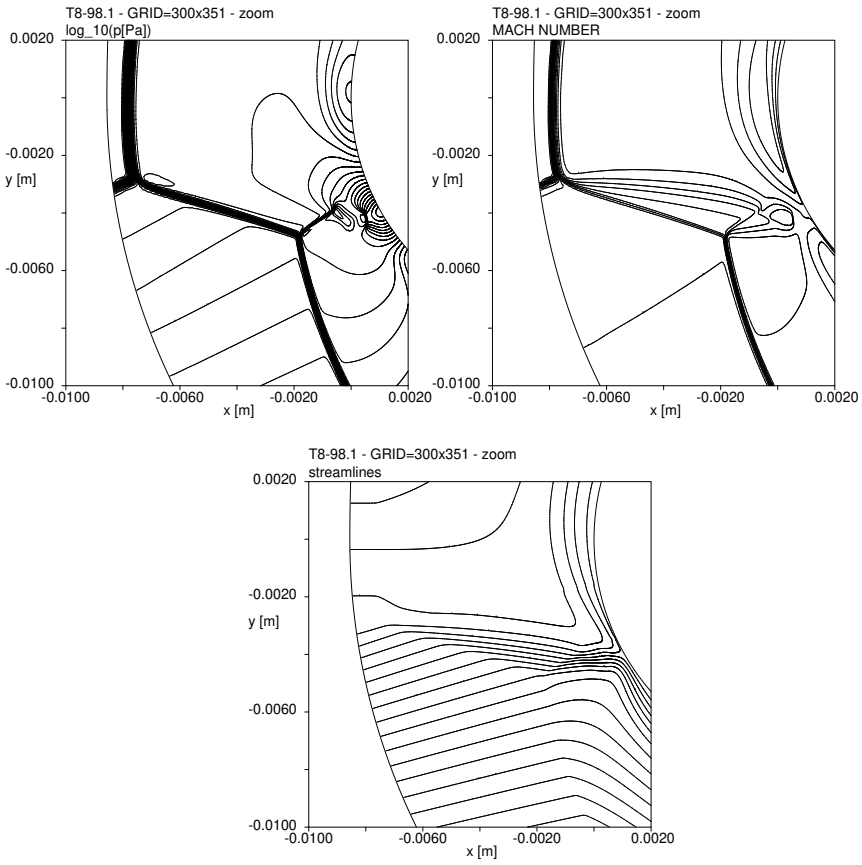

Figure 11 Log_{10} of pressure, Mach number and streamline function contours in the interaction region.

through the detached shock in front of the body. This last pressure rise is smoother for the upper streamline than for the lower one, because the former crosses the detached shock at its margins, where it is just starting to appear, created by converging compression waves.

A larger scale view of the interaction is shown in figure 11. Notice that the position of the cylinder bow shock is completely different with respect to the undisturbed case, being the shock layer thickness of the upper portion more than doubled.

Pressure and heat flux distributions at the wall are shown in figure 12, where they are also compared with results of experiments conducted in the ONERA R5Ch low density wind tunnel [9]. The comparison appears to be rather good. Concerning the level of

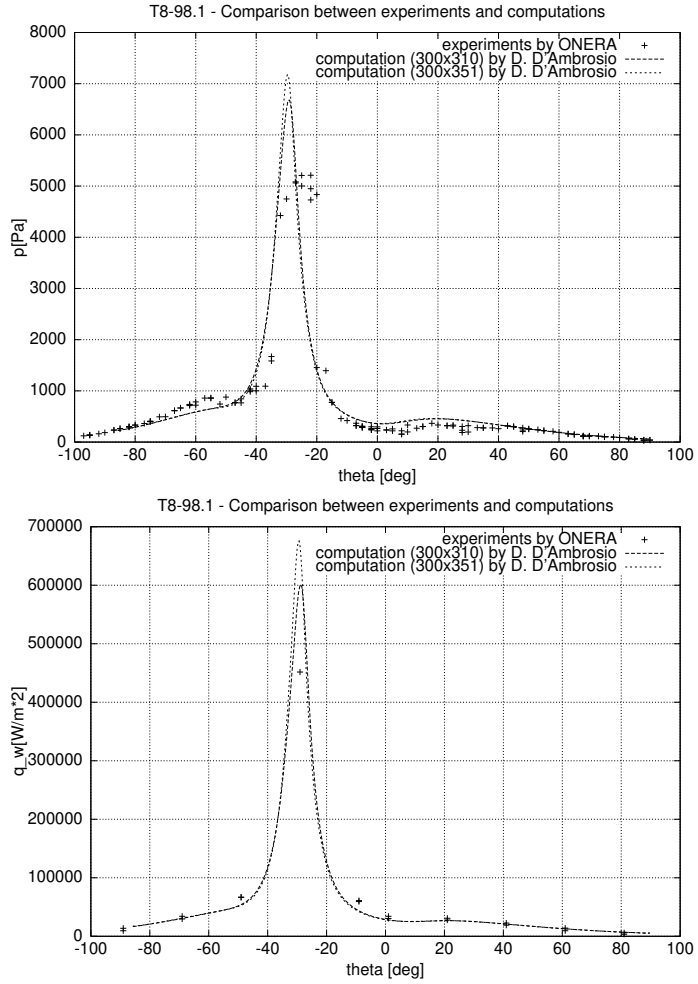

Figure 12 Pressure and heat flux distribution at the wall.

the pressure peak, we explain the higher value displayed by the numerical simulation with the bad spatial resolution of the experiments, due to the fact that in the latter the diameter of the pressure holes is rather large (1.5 mm) [10]. The situation is improved for the heat fluxes, since the diameter of the thermocouples is now smaller (0.4 mm).

The three couples of pictures shown in figure 14 represent the density and temperature distributions along horizontal lines placed 2, 4 and 5 millimeters below the axis of the cylinder. Such lines are superimposed on the density contours in figure 13. The experimental data [9] were obtained using the Dual-line Coherent Anti Stokes Scattering technique (DL-CARS). Also in this case, the comparison is qualitatively rather good. The major differences, for which we have no explaination, concern the stand-off distance of the bow shock portion which is placed over the interference point ($y = -2$mm) and the position of the Mach stem ($y = -4$mm). Such discrepancies are puzzling, since other numerical data, such as wall pressure and heat flux, are in very good agreement with the experimental results. Of course, one may indicate many error sources (in the experiment and in the computation) that could be responsible for such differences in an otherwhise very satisfactory comparison. A possible explaination, where we suppose that the experimental data are correct, could be the following. Looking at the wall pressure plot, we see that the experimental peak is located about 3 degrees more northern than the numerical peak. This could mean that there is a very small error in the position of the impinging shock. If we imagine to move the numerical interaction point a little upwards, we can predict a new Mach stem position closer to the experimental results and we can suppose that possibly also the stand-off distance of the upper and lower bow shock portions could slightly decrease.

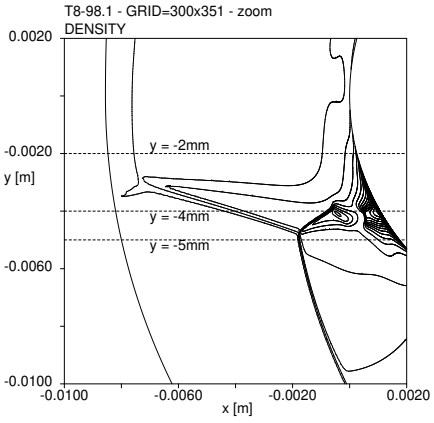

Figure 13 Density contours in the interaction region. Dashed lines indicate DL-CARS experimental data locations.

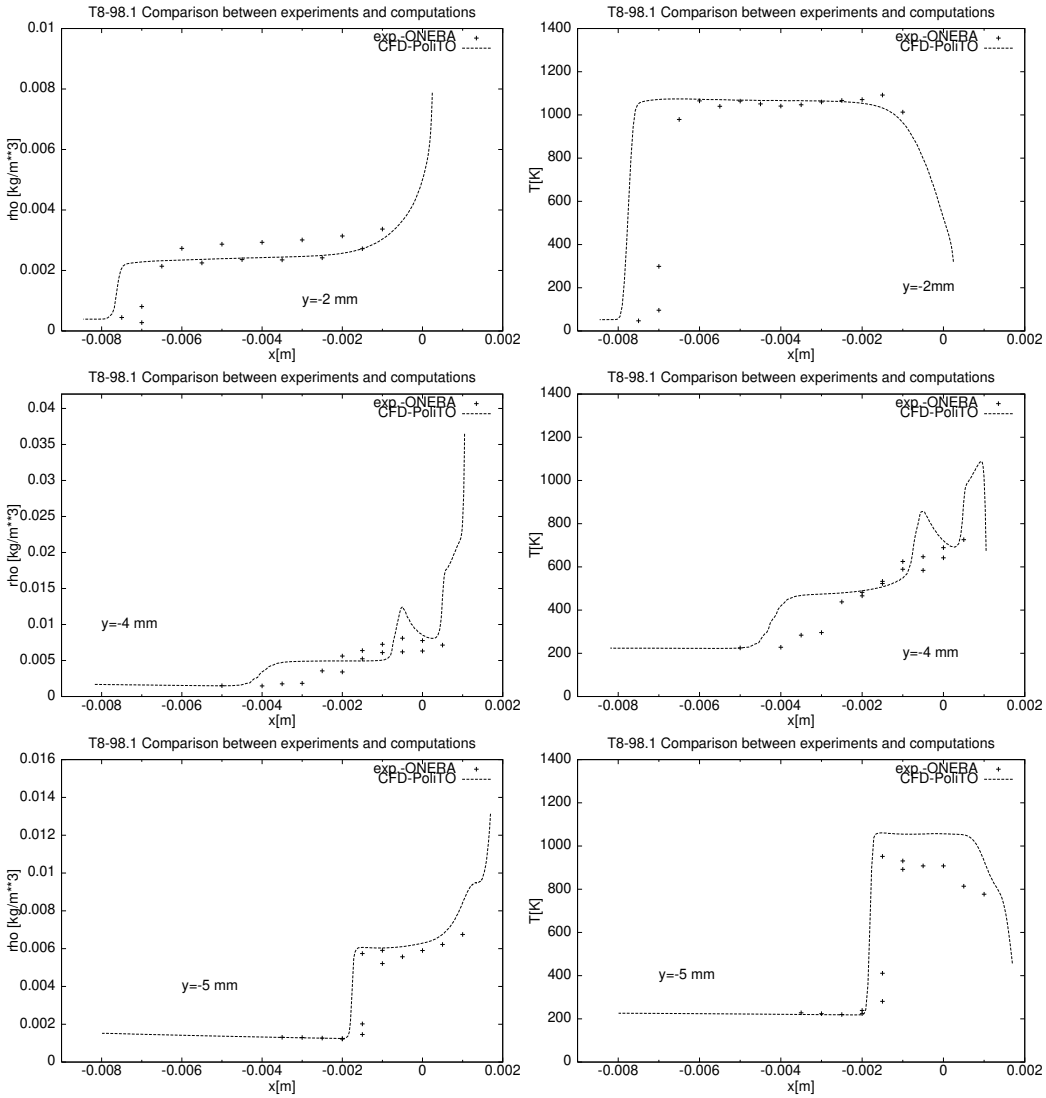

Figure 14 Density and temperature distribution at various $y = const$: computations vs. experiments.

5 Conclusions

Despite the enormous capabilities developed by CFD, the application of the numerical methods for fluid dynamics still requires the careful attention of the researchers, especially in those configurations characterized by complex and challenging fluid dynamics features. Grid convergence, simulation of the correct boundary conditions, establish-

ment of a steady state solution or aknowledgement of the unsteadyness of the flow must be clearly verified for a successful numerical simulation.

References

[1] M. M. S. Borrelli, F. Grasso and J. Periaux, eds., *Fist Europe-US High Speed Flow Field Database Workshop - Part II*, (Naples, Italy), CIRA, AIAA, November 1997.

[2] *East-West High Speed Flow Field Database Workshop*, Vieweg Series: Notes on Numerical Fluid Mechanics, 1998.

[3] D. D'Ambrosio and M. Pandolfi, "Contribution to problem T1-97.1: Hyperboloid-Flare (cold)," in *First US-Europe High Speed Flow Field Database Workshop - Part II* (S. Borrelli, F. Grasso, M. Marini, and J. Periaux, eds.), (Naples, Italy), American Institute of Aeronautics and Astronautics (AIAA), 12-14 November 1997.

[4] D. D'Ambrosio and M. Pandolfi, "Contribution to problem T2-97: Hollow cylinder-Flare," in *First US-Europe High Speed Flow Field Database Workshop - Part II* (S. Borrelli, F. Grasso, M. Marini, and J. Periaux, eds.), (Naples, Italy), American Institute of Aeronautics and Astronautics (AIAA), 12-14 November 1997.

[5] D. D'Ambrosio and M. Pandolfi, "Contribution to problem T4-97: Corner flow," in *First US-Europe High Speed Flow Field Database Workshop - Part II* (S. Borrelli, F. Grasso, M. Marini, and J. Periaux, eds.), (Naples, Italy), American Institute of Aeronautics and Astronautics (AIAA), 12-14 November 1997.

[6] M. Holden, "Experimental Database for CFD Validation for RTO Working Group 10," tech. rep., CALSPAN - University of Buffalo Research Center, June 1999.

[7] H. Schlichting, *Boundary-Layer Theory*. New York: Mc Graw-Hill Book Company, sixth ed., 1968.

[8] B. Edney, "Anomalous heat-transfer and pressure distributions on blunt bodies at hypersonic speeds in the presence of an impinging shock," FFA Rept. 116, Aeronautical Research Inst. of Sweden, Stockholm, Sweden, February 1968.

[9] J. Moss, T. Pot, B. Chanetz, and M. Lefebvre, "Dsmc simulation of shock/shock interactions: emphasis on type iv interactions," in *22nd International Symposium on Shock Waves*, (London, Great Britain), July 18-23 1999.

[10] T. Pot, November 1998. private communication.